

GT2011-4) - +-

AERODYNAMIC AND AEROTHERMAL INVESTIGATION OF THE FLOW AROUND AN HPT ROTOR SHROUD: HEAT TRANSFER AND COOLING EFFECTIVENESS

Knut Lehmann, Vasudevan Kanjirakkad, Howard Hodson
 Whittle Laboratory, University of Cambridge
 Cambridge CB3 0DY, UK

ABSTRACT

An experimental study has been conducted to investigate the aerothermal performance of a shrouded high pressure turbine blade in a large scale rotating rig. The rotor blade and the associated shroud and casing geometry have been modelled in a large scale low speed turbine rig that was designed to investigate a novel passive shroud cooling methodology.

The objective of the present paper is to describe the aerothermal performance of a passive shroud cooling strategy using measured heat transfer and adiabatic cooling effectiveness data. Improved physical understanding of the shroud aerodynamics as reported in the companion paper Lehmann et al. [1] will be used here to support the analysis.

Highly resolved experimental heat transfer data was acquired on the shroud, the fins and on the shroud underside with the thin heater film method. The distribution of the adiabatic cooling effectiveness on the rotor shroud was measured with a combination of the Ammonia-Diazo and a foreign gas sampling technique. The measurements are complemented by steady numerical computations of the turbine stage.

Due to the impact of vortical flow structures in the over shroud cavities, the Nusselt numbers on the shroud top surfaces were found to be of the same order as on the shroud underside. The passive shroud cooling concept was found to provide quite efficient and uniform cooling to the over-shroud surfaces while the distribution of coolant on the shroud underside was significantly affected by the rotor secondary flow.

NOMENCLATURE

Greek symbols

γ	Electrical conductivity	$[\text{m}\Omega^{-1}\text{mm}^{-2}]$
μ	Dynamic viscosity	$[\text{Pa s}]$
η	Cooling effectiveness	$[-]$
ρ	Density of air	$[\text{kg m}^{-3}]$
ϕ	Flow coefficient	$[-]$

Latin symbols

C_{stator}	Stator midspan chord	$[\text{mm}]$
C_{rotor}	Rotor midspan chord	$[\text{mm}]$
C	Concentration	$[\text{ppm}]$
h	Heat transfer coefficient	$[\text{Wm}^{-2}\text{K}^{-1}]$
k	Thermal conductivity	$[\text{Wm}^{-1}\text{K}^{-1}]$
\dot{m}	Mass flow rate	$[\text{kg s}^{-1}]$
Nu	Nusselt number	$[-]$
\dot{q}	Heat flux density	$[\text{Wm}^{-2}]$
Re	Reynolds number	$[-]$
T	Temperature	$[\text{°C}]$
U	Blade speed at midspan	$[\text{ms}^{-1}]$
V	Velocity, absolute	$[\text{ms}^{-1}]$
W	Velocity, relative	$[\text{ms}^{-1}]$

Subscripts

0	stagnation value
1	at stator inlet
2	at rotor inlet
3	at rotor exit
aw	adiabatic wall
iw	impermeable wall
x	axial

INTRODUCTION

A major benefit of shrouded high pressure turbines is the high durability of the rotor tip clearance. However, the weight of the shroud increases the mechanical stresses in the entire blade-disk assembly and thus limits the speed and work output of the turbine. Lighter shrouds are therefore desirable. Kanjirakkad et al. [2] and Janke et al. [3] have recently investigated passive shroud cooling concepts to avoid thick shrouds with active internal and film cooling. An improved ‘through platform’ cooling concept was derived which has superior aerodynamic and cooling performance compared to conventional cooling methods.

Besides the cooling effectiveness, the external heat transfer coefficient is important when determining the life of turbine blading. It also highlights regions where cooling is necessary. Information concerning the heat transfer coefficients on shrouded turbine blades is scarce but such data is very important to further improve shroud cooling methods and shroud designs. Some shroud equivalent heat transfer data is available from the labyrinth seal literature e.g. Waschka et al. [4] and Wittig et al. [5]. These authors have investigated straight-through and stepped labyrinth seals. They report high heat transfer on the front faces and tip of the fins and relatively low heat transfer in the cavities. Haller and Hilditch [6] recently presented experimental heat transfer data for the underside of a HPT shroud. They also concluded from computations that the heat transfer coefficient along the over-shroud leakage path is very low. The heat transfer measurements of Lehmann et al. [7] contradict this finding. The authors show that the small inter-shroud gaps have a decisive impact on the flow structure and heat transfer in the shroud cavities.

The purpose of this investigation is to provide a detailed assessment of the aerothermal performance of an engine-representative high pressure turbine shroud. The results show distributions of the Nusselt number and cooling effectiveness that were obtained from a large scale rotating turbine rig as well as from numerical investigations. The results are explained with the knowledge obtained from the aerodynamic investigation of shroud leakage flows that is presented in a companion paper, Lehmann et al. [1].

EXPERIMENTAL METHOD

Configuration of the research turbine

The large-scale low-speed research turbine at the Whittle Laboratory, also known as the Peregrine rig, was used to perform an experimental study of the rotor shroud flows in a single stage shrouded HPT configuration. The principal layout of the test section is sketched in Figure 1. Some important geometrical parameters as well as the operating conditions of the turbine are listed in Table 1.

A large variable speed suction fan pulls the flow through the turbine stage. The power generated by the turbine is absorbed

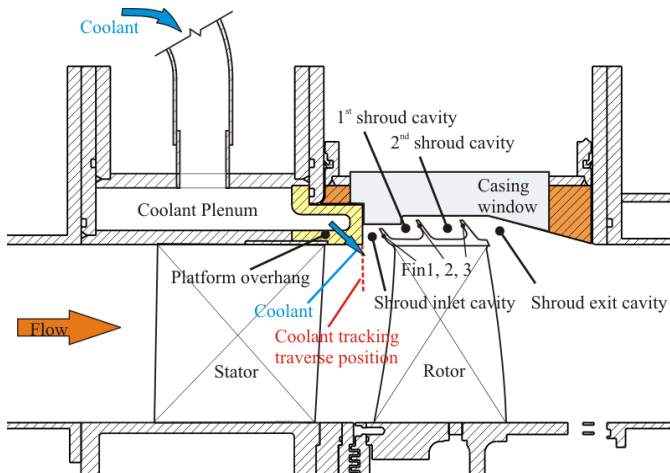


Figure 1 Schematic of the research turbine

Number of stages	1
Number of stator blades	26
Number of rotor blades	45
Mean radius [m]	0.6858
Hub-tip radius ratio	0.8
Stator chord (mid-span) [mm]	225
Rotor chord (mid-span) [mm]	120
Rotor tip clearance (nominal) [%span]	1.4
Inter-shroud gap size (nominal) [mm]	1.3
Number of coolant holes	260
Coolant hole diameter [mm]	4
Coolant flow rate $m_{\%cool} = m_{cool}/m_{inlet} \times 100$	0.75%–3%
Blowing ratio $M = \rho_{cool} V_{cool} / \rho_2 V_2$	0.5–2
Flow coefficient $\phi = V_{x1} / U$	0.42
Re (nominal) $Re = \rho_1 (V_{x1} / \cos 70^\circ) C_{stator} / \mu$	5×10^5
Re (rotor based) $Re_R = \rho_3 W_3 C_{rotor} / \mu$	2.5×10^5
Rotational speed [rpm]	~360
Near-casing Stator flow angles (inlet/exit) [°]	0° / 67°
Near-casing Rotor flow angles (inlet/exit) [°]	-2° / -62°

Table 1 Geometrical parameters and test conditions

by an eddy current brake, which in turn is used to control the rotational speed of the turbine rotor. The fan and brake are in a control loop such that the rig operating condition (Re and ϕ) is accurately controlled within $\pm 0.5\%$ during an experiment.

The stage consists of 26 stator and 45 rotor blades. Each rotor blade carries a shroud with three forward leaning fins. Inter-shroud gaps of 1.3mm width separate the individual rotor shrouds in the circumferential direction. The rotor casing above the shroud consists of a parallel annulus with a backward facing step in front of the first and the second fin.

The stage configuration features the passive ‘through platform’ cooling concept (Kanjirakkad [2]). Coolant air is ejected through 260 circular holes in the stator platform overhang at a tangential angle of 65° with a radial compound angle of 30°. The ejection occurs 12 mm (three hole diameters) upstream of the shroud inlet cavity. The cooling concept is intended to cool the over-shroud region as well as the shroud underside.

Heat transfer measurement technique

A steady-state TLC (Thermochromic Liquid Crystal) heat transfer measurement technique using thin heater foils was chosen for the experiment. The turbine blade used was manufactured from Polyurethane (AXSON PX245) which has a thermal conductivity of 0.2 Wm⁻¹K⁻¹. About 1.5 mm of this material was machined from both sides of the turbine shroud and replaced by copper bus bars machined to match the shroud profile as shown in Figure 2a. Thin metal heater foils were implemented on all 1-D curved surfaces of the shroud. Two types of metal foils were used to manufacture the heater foils. These are listed in Table 2. The ‘ultra thin’ foils have the advantage of low current requirements, fast responsiveness and excellent representations of thermal gradients. However, due to their higher durability, the ‘super thin’ foils have proven to be more reliable in the current application.

Type	Thickness [μm]	Electr. cond. [$\text{m}\Omega^{-1}\text{mm}^{-2}$]	Th. cond. [$\text{Wm}^{-1}\text{K}^{-1}$]	Material
“ultra thin”	2.54	0.73	11.2	EvanohmS
“super thin”	12.7	0.971	14.8	Inconel 600

Table 2 Material properties of the heater foils

Three different heat transfer blades were manufactured (see Figure 2). Blade 1 was equipped with heater foils on the bottom faces of the shroud cavities as well as the rear surfaces of the fins. Blade 2 had heater foils attached to the front faces of the fins. To cover the shroud underside (Blade 3) in the same manner, a more difficult concept had to be used. In order to run the heater foils between the two bus bars on either sides of the shroud, the shroud was separated from the blade. Five strips of heater foil were attached to the shroud underside. The shroud was then assembled to the blade using long screws. As the heater foils under the blade profile cannot convectively dissipate heat, an electrically insulated metal spacer was placed between the blade and the shroud. The thickness was chosen such that its surface area exposed to the flow is equal to the area of heater foil it covers.

Optical access to the top surfaces of the shroud (Blade 1 and Blade 2) was provided by a Perspex window in the rotor casing, see Figure 1. In order to capture clear images of the instrumented heat transfer blade, a high speed stroboscopic light source was used. For the image acquisition on Blade 3, cameras

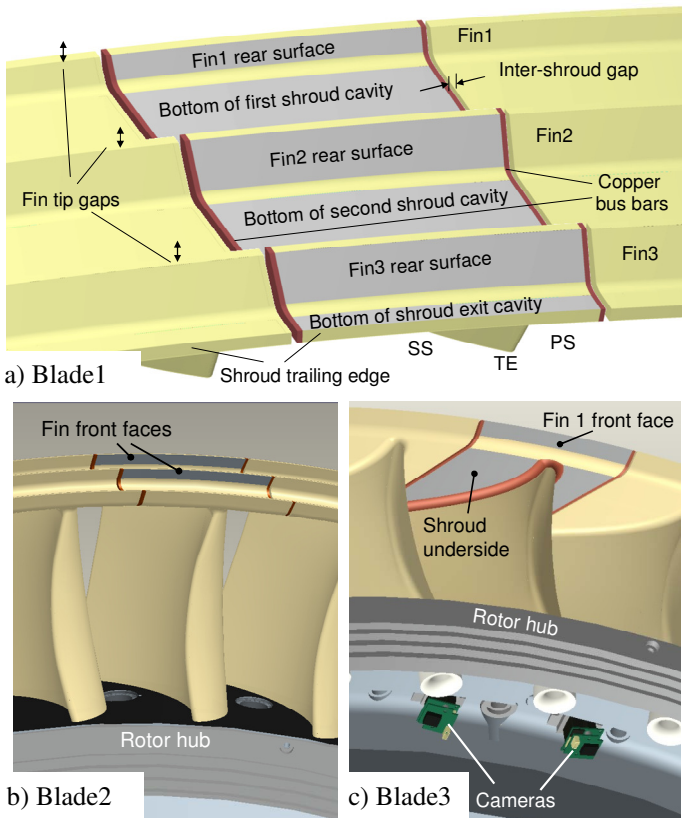


Figure 2 Schematics of the heat transfer measurement blades

and lighting were implemented into the rotor hub such that the shroud could be viewed from the rotating frame of reference (Figure 2c).

Two narrow-band Thermochromic Liquid Crystals (TLC) of type Hallcrest BM/R35C1W and BM/R50C1W were used in a 1:1 mixture. The mixture was calibrated in a hot water bath. The yellow line temperatures were found to be approximately 35°C and 49°C respectively. Additionally, an in-situ calibration was performed with a foil thermocouple attached to one heated shroud surface. Good agreement between both calibrations was achieved.

For this steady state heat transfer measurement technique using a narrow band TLC, a full map of isothermals (yellow TLC contours) is required on the heater foils. In practice, this is achieved by acquiring images for a range of power settings to the heater foils \dot{q}_{gen} (typically 0-6000Wm⁻² in 100 steps). A semi-automated procedure was used to digitize the temperature information from the images.

The local heat transfer coefficient is defined as:

$$h = \frac{\dot{q}_{conv}}{T_{TLC} - T_{aw}} \quad \text{with} \quad \dot{q}_{conv} = \dot{q}_{gen} - \dot{q}_{cond} - \dot{q}_{rad} \quad (1)$$

where \dot{q}_{conv} is the local convective heat flux from the heater foil into the flow and \dot{q}_{cond} and \dot{q}_{rad} are heat losses due to conduction and radiation respectively. The local adiabatic wall temperature T_{aw} was measured with thermocouples in the four shroud cavities. The heat transfer coefficient is then further reduced and presented as the dimensionless Nusselt number.

$$\text{Nu} = \frac{hC_{rotor}}{k_{air}} \quad (2)$$

The experimental uncertainty in the Nusselt number is dominated by conduction losses and was estimated to be less than 14%. A more detailed description of the experimental setup and the data reduction method is reported in Lehmann et al. [7] and [8].

Adiabatic cooling effectiveness measurements

The adiabatic cooling effectiveness is a ratio of temperatures defined as:

$$\eta_{cool,aw} = \frac{T_{aw} - T_{\infty}}{T_{coolant} - T_{\infty}} \quad (3)$$

Using the analogy between heat and mass transfer in turbulent flow, a foreign gas technique may be employed to measure the adiabatic cooling effectiveness. The Ammonia-Diazo technique ([9], [2]) was used in the present study. The technique relies upon the chemical reaction (darkening of the diazo foil) that occurs when it comes in contact with ammonia gas. Prior to the experiments, the surfaces of the shroud are coated with Diazo foil. The measurements take place while small amounts of ammonia are mixed into the coolant flow. Over time (typically two hours) the Diazo foil darkens according to the local ammonia concentration in the flow. In the case of negligible free stream concentration, the relative darkness of the Diazo foil is representative of the relative

ammonia concentration at the wall and hence of the adiabatic cooling effectiveness.

$$\eta_{cool,aw} = \frac{C_{iw} - C_{\infty}}{C_{coolant} - C_{\infty}} = \frac{C_{iw}}{C_{coolant}} \quad (4)$$

For the calibration of foil darkness vs. concentration a separate experiment is performed in a similar manner. Small amounts of ethylene are continuously seeded into the coolant plenum. Gas samples are taken from the coolant plenum and also from pressure tappings at various positions on the shroud. The gas samples are then tested for their ethylene concentration using an ionizing gas analyzer. Thus a quantitative calibration of the Ammonia-Diazo experiment is achieved. The uncertainty in the results is approximately 10%.

In a separate experiment ethylene seeded coolant was also used to determine the distribution of coolant at the inlet of the rotor passage. A small Pitot probe was traversed in the outer 10% span of the passage and used to sample the flow.

NUMERICAL METHOD

Mixing plane calculations of the turbine stage were performed using FLUENT6.3 with the realizable k-ε turbulence model. The mesh, created in CENTAUR, is unstructured with prismatic cells near the walls. It has a size of 10.5 million cells with an increased cell density along the shroud leakage path. The y^+ values on the shroud are less than unity throughout. A cut through the mesh in the shroud region is shown in Figure 3.

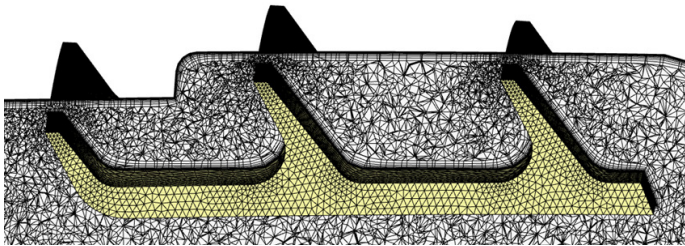


Figure 3 Computational mesh in the shroud cavities

The calculations of the heat transfer coefficient were performed to mimic the experiments as closely as possible. For that reason, the different heater foil configurations on ‘Blade 1-3’ were simulated in three different computations. Only the surfaces that were covered by the heater foils in the respective experiments were imposed with the corresponding heat flux boundary condition. More details on the numerical method are reported in Lehmann et al. [7].

For the numerical prediction of the adiabatic cooling effectiveness, the coolant flow temperature was used as a tracer for the coolant flow. It was set to be 20 K higher than the mainstream temperature. This value was chosen as a compromise between two constraints. A high value is desired to minimise the influence of numerical errors as well as errors from temperature changes resulting from the work extraction in the turbine. On the other hand the density changes should be small in order to avoid buoyancy effects and changes in the blowing ratio of the coolant flow.

RESULTS AND DISCUSSION

Heat transfer on shroud top surfaces

The Nusselt number distribution on the top surfaces of the shroud were published by Lehmann et al. [7]. The data for the uncooled baseline condition is repeated here and presented together with the shroud flow model (from companion paper [1]) in Figure 4.

The leakage flows from the fins and the inter-shroud gap as well as the relative flow direction in the shroud cavities are illustrated with arrows. The tangential component of the cavity flows is about 75 % of the blade speed and thus against the direction of rotation in the blades’ reference frame. The leakage flow that enters the shroud cavities through the inter-shroud gap radially is turned by this swirling cavity flow and convects with it along the shroud cavities. In a very simplified view, this results in the start of a fresh thermal boundary layer at the suction side of the shroud. As the cavity flow develops towards the pressure side of the shroud, the boundary layer grows causing a general decrease of the Nusselt number in this direction.

In the first shroud cavity, the leakage flow from the inter-shroud gap triggers the separation of the fin tip leakage jet from the rotor casing. Subsequently, the fin tip leakage jet attaches on the bottom of the first cavity and rolls up into the shroud cavity

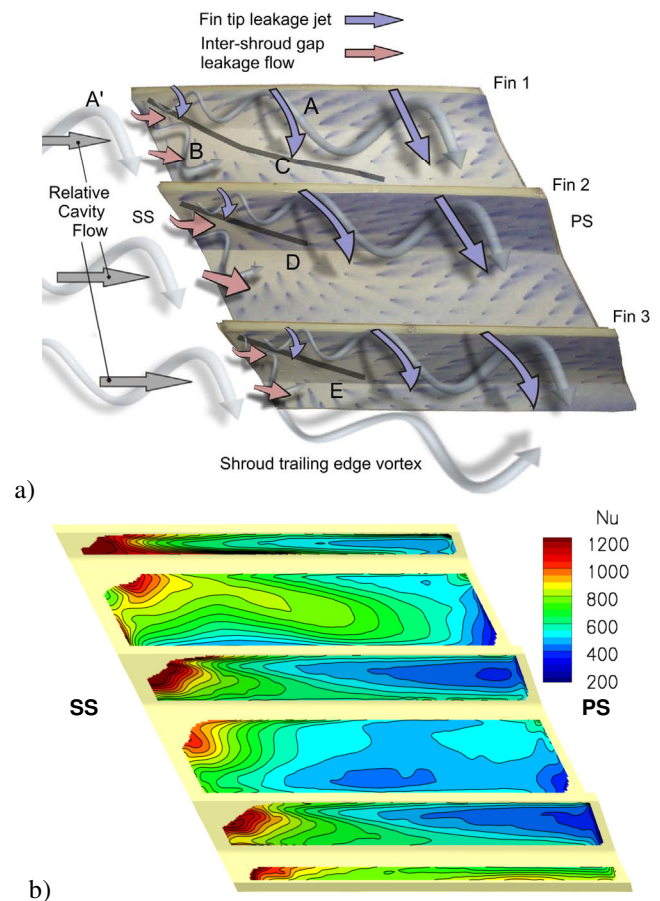


Figure 4 Flow visualisation and measured Nusselt number distribution on the top surfaces of the shroud for the uncooled case

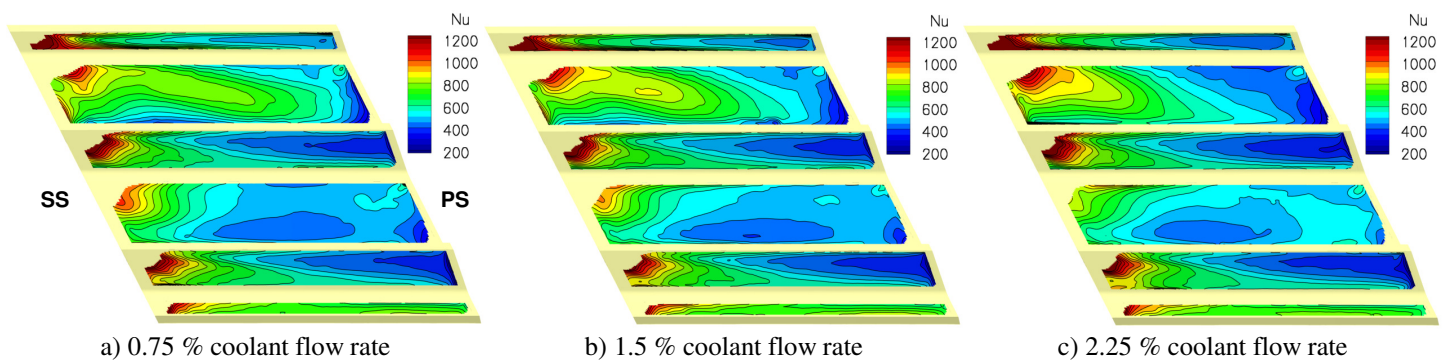


Figure 5 Effect of the coolant flow rate on the measured Nusselt number distribution of the shroud top surfaces

vortex A. The attachment of this flow along line C causes a long tongue shaped region of high Nusselt numbers. Especially at the rear surface of Fin 1 near the inter-shroud gap, the Nusselt numbers are extremely high. This region is dominated by the interaction of two vortices, namely the shroud cavity vortex A and the inter-shroud gap vortex B (see Figure 4). Both vortices are driven by leakage jets. They feed fin tip leakage flow and inter-shroud gap leakage flow directly onto the shroud surface, thus causing the increased Nusselt numbers.

The driving mechanisms and therefore the flow structures that are present in the second shroud cavity and the shroud exit cavity are very similar to those found in the first shroud cavity. The tangential velocity of the swirling cavity flow is similar in all three cavities. However, in the second and the exit shroud cavities, the leakage flow fractions are slightly changed towards more fin tip leakage and less ingestion from the inter-shroud gap. Consequently, the separation of the fin tip leakage jets and the trajectory of the shroud cavity vortices are slightly altered. The Nusselt contours show sharp kinks on the rear faces of both fins that correlate very well with the attachment lines D and E, observed in the flow visualisation (see Figure 4a). A main difference to the first shroud cavity is that the second cavity and the exit shroud cavity have larger radial dimensions (taller fins). Thus, the shroud cavity vortex does not reach the bottom surface and the heat transfer augmentation is largely confined to the rear surfaces of Fin 2 and 3.

Apart from the suction side, the narrow bottom surface of the shroud exit cavity also exhibits high Nusselt numbers near the pressure side of the shroud. This region is characterised by the interaction of the shroud cavity and the shroud trailing edge vortex (see companion paper [1], Figure 11). Both vortices feed flow onto the shroud causing high Nusselt numbers.

The effects of the coolant flow rate on the Nusselt number are presented in Figure 5. The coolant flow modifies the near casing inflow to the rotor. A coolant flow rate of 1.5 % (Figure 5b) is the design case and corresponds to a blowing ratio of approximately unity. Hence, the relative inflow angles to the rotor and the Nusselt distribution are approximately equal to the uncooled case. Off design coolant flow rates modify the relative inflow angles to the rotor which is essentially equivalent to a change in the local flow coefficient. The effect is most pronounced in the first shroud cavity. The trace of high Nusselt numbers, formed by the impingement of the cavity vortex, is slightly longer for 0.75 % coolant flow rate. In this case, the

relative tangential velocity of the cavity flow is higher and thus the separation of the fin tip leakage jet from the rotor casing occurs closer to Fin 1. The opposite is true for coolant flow rate of 2.25 %. Here the circumferential velocity in the first shroud cavity is closer to the blade speed. Consequently, the separation of the fin tip leakage jet from the casing is shifted away from the fins.

Cooling effectiveness on the shroud top surfaces

The coolant air, which is injected through the 260 discrete holes in the stator platform overhang (see Figure 1) undergoes a mixing process with the main passage flow. The distribution of coolant just upstream of the shroud inlet cavity is shown for the design coolant flow rate of 1.5 % in Figure 6. A layer of high coolant concentration is clearly visible near the casing. The coolant jets undergo a stronger mixing with the overturned flow near the suction side of the stator wake. Near the pressure side of the wake, the injection angle of 65° is better aligned with the passage flow. This causes less mixing and the trace of the individual jets are still visible.

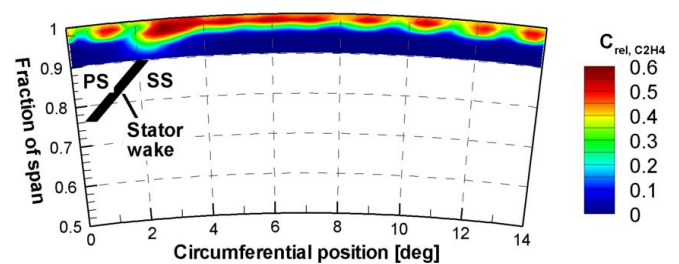


Figure 6 Coolant tracking at rotor inlet at 1.5 % coolant flow rate (rel. C₂H₄ concentration measured)

The experimental results of the cooling effectiveness along the over-shroud leakage path, i.e. on the shroud top and fin surfaces are presented in Figure 7 together with the numerical predictions. (The figures show the unfolded surfaces of the shroud.)

For the design coolant flow rate of 1.5 %, Figure 7b, the effectiveness values are fairly uniform in the first shroud cavity. An influence of the impinging fin tip leakage jet, as found in the heat transfer results, is not observed. This suggests that the coolant concentration in the leakage jet from Fin 1 does not vary greatly in the circumferential direction. The only non-uniformity is found at the suction side near the front face of Fin 2. In this region, main passage fluid is ingested from the

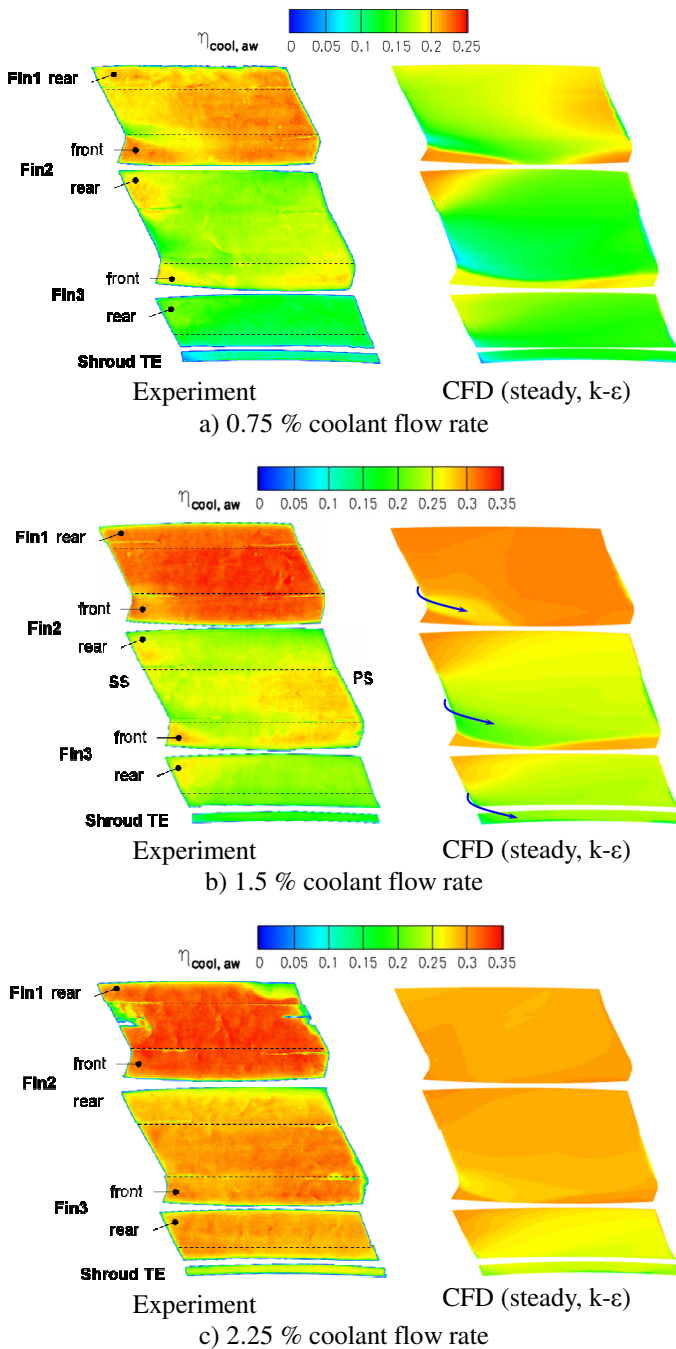


Figure 7 Cooling effectiveness on the shroud top surfaces

inter-shroud gap (marked by arrow in Figure 7b). Since this fluid has lower coolant concentrations than the cavity flow, a streak of low effectiveness values reaches from the inter-shroud gap towards the front face of Fin 2. Although visible in both experiment and CFD, the effect appears to be slightly stronger in the predicted results. This is assumed to be related to slight differences in coolant concentration on the shroud underside (see Figure 11).

Compared to the first cavity, the cooling effectiveness is significantly reduced in the second shroud cavity. The cavity flow is diluted by inter-shroud gap leakage flow which contains less and less coolant as it originates from positions further

downstream on the shroud underside. The front face of Fin 3, particularly its tip section, remains surprisingly well cooled as it is mainly under the influence of the highly cooled tip leakage jet that is carried over from Fin 2. As in the first shroud cavity, the poorly cooled leakage flow from the inter-shroud gap causes a streak of low effectiveness near the root of Fin 3. The cooling effectiveness is further reduced in the shroud exit cavity. Both the inter-shroud gap leakage and the ingestion and recirculation of main passage fluid in the shroud exit cavity lead to a decreased concentration of the coolant.

A coolant distribution similar to that described above is found for the off design coolant flow rate of 0.75 % albeit with lower effectiveness values, see Figure 7a. Some differences between experiment and CFD are found in the first cavity. The leakage from the inter-shroud gaps appears to have lower concentrations in the predicted results. Thus, the mixing of cavity flow with the main passage flow leads to slightly lower effectiveness values.

At 2.25 % coolant flow rate (Figure 7c) the streaks of low effectiveness values resulting from inter-shroud gap leakage almost disappear. This is a consequence of the improved coolant coverage on the aft part of the shroud underside. Uniform cooling with effectiveness values near 0.3 are achieved in first and second shroud cavity. The anomalies in the experimental results in the first cavity (low effectiveness regions) are related to an accidental damage of the Diazo foil during the removal of the Diazo foil from the shroud.

Heat transfer on shroud underside

The results of the Ammonia-Diazo flow visualisation experiments on the shroud underside are presented in Figure 8 together with the predicted results for the uncooled case. The agreement between the results is very good. The secondary flows appear to be quite weak on the shroud underside. This is due to the fact that the stator exit casing boundary layer is, at least, partially removed into the shroud inlet cavity (see companion paper [1], Figure 4c). Furthermore, the freshly developed endwall boundary layer on the pressure side of the shroud is bled into the inter-shroud gap. The reduced overturning downstream of the inter-shroud gap can be seen in both the numerical and the experimental results.

The heat transfer measurements on the shroud underside were performed using the instrumented ‘Blade 3’ as shown in Figure 2. The blade allowed obtaining heat transfer data on the entire shroud underside with the exception of the fillet area near Fin 1. A set of heat transfer data for the shroud underside is presented in Figure 9a.

The incoming flow to the shroud leading edge consists of near casing flow from stator exit. This boundary layer flow is at least partially drawn into the shroud inlet cavity. A stagnation line forms on the shroud leading edge, see Figure 8. A fresh boundary layer develops thereafter on the shroud underside. This leads to high Nusselt numbers at and directly downstream of the stagnation line. It has to be noted that the heating starts about 1/10 axial chord downstream of the stagnation line. Hence, there is no data available directly in the stagnation region. On the pressure side, the Nusselt numbers drop quickly

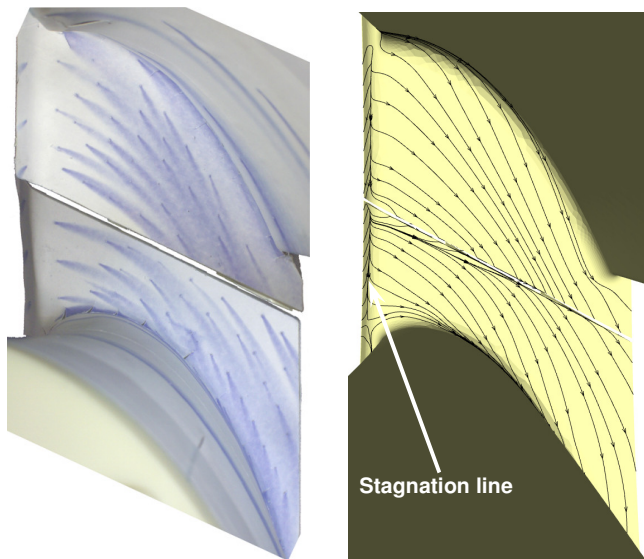


Figure 8 Flow visualization on the shroud underside

from about 800 to about 400 as a thermal boundary layer develops. The Nusselt numbers remain at low levels and show a quite uniform distribution until the trailing edge of the shroud. Close to the pressure surface of the blade, the Nusselt numbers increase slightly as a result of radially outwards moving fluid on the blade pressure side.

On the shroud suction side, where the velocities are higher, the Nusselt numbers drop from about 1000 near the shroud leading edge but stay at a fairly high level of about 600 in the region downstream.

Up to about half an axial chord downstream of the blade leading edge, the flow in the passage is nearly parallel to the inter-shroud gap. Further downstream, the flow angle is higher and fluid passes from the pressure side of the neighbouring shroud onto the suction side of the heated shroud (compare with flow visualisation Figure 8). A substantial part of the boundary layer flow, which had developed on the neighbouring shroud, is sucked into the inter-shroud gap. A new boundary layer is formed from cold and high momentum flow. This leads to high initial Nusselt numbers that are greater than 1200 that then reduce quickly to about 500 as the flow progresses towards the blade suction surface. The near surface flow in this region is characterised by some overturning. In the region near the blade trailing edge, the Nusselt numbers increase again. There is a spot of high Nusselt numbers directly behind the blade trailing edge. This is likely a result of the interaction between the blade wake and the shroud boundary layer.

Along the pressure side and suction side edge of the heated shroud, the Nusselt numbers alternate between higher and lower values. A closer inspection shows that there appears to be one spot of high and low Nusselt number per heater foil. Higher Nusselt numbers are found in the obtuse corners of the heater foils and lower Nusselt numbers are found in the acute corner respectively. This effect is a result of a slightly non-uniform heat flux distribution from the heater foils. However, it has to be noted that the measured heat transfer coefficient is not inaccurate. It merely represents a true response to the imposed thermal boundary condition. These effects appear also in CFD

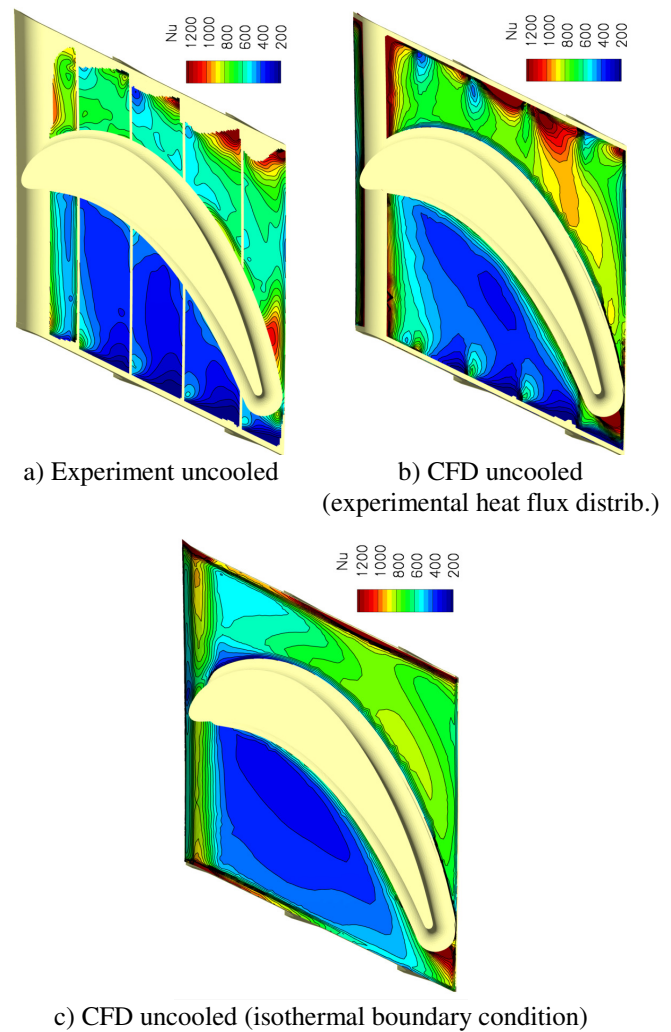


Figure 9 Distribution of Nusselt number on the shroud underside

calculations that simulate the thermal boundary condition of the experiment, Figure 9b. The CFD results are in good agreement with the experiments and support the conclusion drawn from the measured results.

Figure 9c shows the predicted Nusselt numbers for an isothermal boundary condition. This more realistic boundary condition does not show the alternation of high and low Nusselt number near the sides of the shroud. However, the general distribution of the Nusselt numbers as well as the magnitude is similar to the experimental results. The biggest difference is near the suction side edge of the shroud where the augmented Nusselt numbers due to the start of a fresh boundary layer are confined to a much smaller region.

Figure 10 shows how the coolant flow influences the Nusselt number distribution on the shroud underside. No significant change was found between the results for 0 %, 0.75 % and 1.5 % coolant flow. This is due to the fact that a substantial portion of the coolant, if injected at a blowing ratio less or equal to one, stays very close to the stator casing and gets drawn into the shroud leakage path. Only at higher coolant flow rates gets the near casing flow energised and contains, in the extreme case of 3 % coolant flow rate, higher momentum

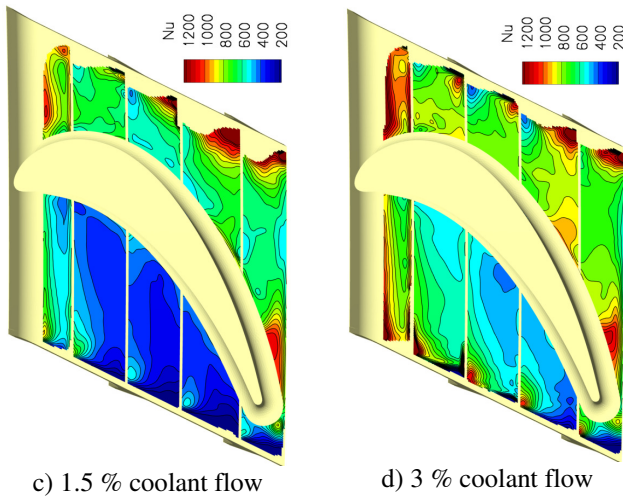


Figure 10 Effect of coolant flows on the distribution of the Nusselt number on the shroud underside

fluid than the passage itself. In the relative frame, this translates into increased positive incidence in the rotor tip region and overturning of the near shroud flow. This yields increased Nusselt numbers on the entire shroud underside. A small exception is the rear part of the shroud suction side near the inter-shroud gap. Since the flow is overturning, it is almost parallel to the inter-shroud gap and hence less flow is crossing over from the neighbouring shroud.

Cooling effectiveness on shroud underside

As shown in Figure 6, the coolant forms a relatively uniform layer near the casing just upstream of the shroud inlet cavity. This flow is partially injected into the shroud inlet cavity and a remainder convects into the rotor passage and provides coolant to the shroud underside.

The experimental results for the cooling effectiveness on the shroud underside are plotted in Figure 11 for the different coolant mass flow rates. Both experimental and numerical results are presented and agree very well. For the lowest coolant flow rate of 0.75 %, only the front part of the shroud underside receives significant amounts of coolant. On its rear part, the effectiveness is quite low. This is a result of a mixing process and also of the secondary flows in the rotor passage. The low cooling flow rate corresponds to a blowing ratio of about 0.5. Thus, the coolant flow has significantly lower momentum compared to stator exit flow. The resulting overturning of the coolant flow on the shroud underside can be seen in Figure 11a. On the suction side of the shroud, this overturning is amplified by fluid that is spilled from the inlet cavity into the rotor passage. This fluid has even lower tangential momentum due to losses in the cavity and presents negative incidence on the rotor blade. On the pressure side part of the shroud underside, the effectiveness values are very low. The coolant is almost completely washed away by the rotor secondary flow near the aft part of the rotor blade.

The cooling effectiveness distribution is not periodic between the pressure side and the suction side of adjacent shrouds. This is due to the leakage flow that leaves the main passage through the inter-shroud gaps. This becomes evident

especially in the aft part of the shroud where the flow crosses the inter-shroud gap from the pressure side to the suction side of the adjacent shroud. This leads to the removal of cooled flow into the shroud cavities resulting in a streak of low effectiveness downstream of the gap on the suction side of the shroud. This effect is strongest with 0.75 % coolant flow rate and visible in both the experimental and the CFD results.

For the case of 1.5 % coolant mass flow rate, a blowing

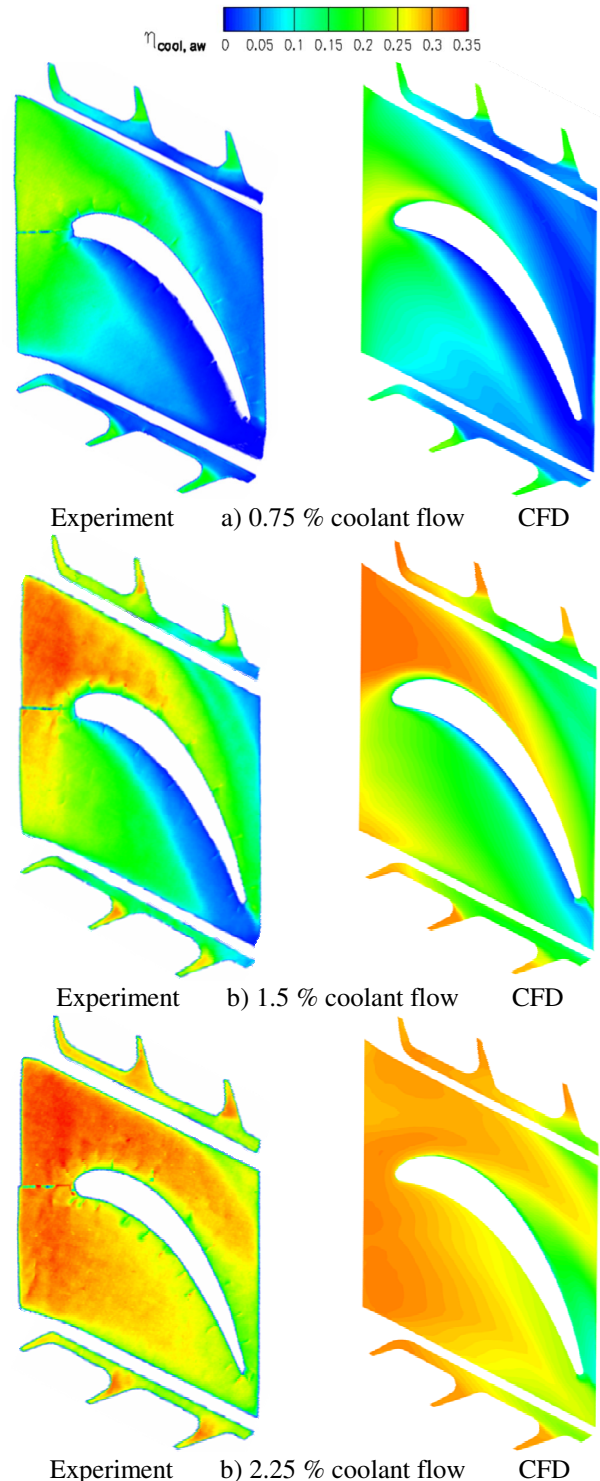


Figure 11 Cooling effectiveness on the shroud underside

ratio of approximately unity is achieved. This results not only in higher cooling effectiveness values but also in a more uniform coverage of the aft part of the shroud underside (Figure 11b). Some overturning of coolant on the shroud underside is still visible near the blade pressure side where uncooled blade boundary layer fluid is washed onto the shroud underside.

It was shown from the PIV measurements that a spiralling vortex is present in the shroud inlet cavity. The mixing that is associated with this vortex might suggest that the cooling effectiveness is very uniform in the shroud inlet cavity and on the front face of Fin 1. However, the experimental and numerical results do not support this hypothesis. Both show a significant variation of the cooling effectiveness on the front face of Fin 1. Despite the strong mixing in the shroud inlet cavity, the suction side receives more coolant flow. This is caused by the potential field of the rotor blade and the resulting inflow/outflow pattern at the shroud inlet cavity (see companion paper [1], Figure 4c). More fluid is being swallowed by the cavity near the blade pressure side. The ingested fluid does not only originate from the highly cooled layer near the stator casing but also contains less cooled flow from lower span-wise positions. Thus, the rotor relative inlet cavity flow is slightly more diluted on the pressure side compared to the suction side. Moreover, near the suction side, the coolant layer passes the shroud inlet cavity interface with little coolant being swallowed. Consequently, this flow can provide much more coolant to the suction side part of the shroud underside.

Further improvements in the uniformity of the coolant coverage on the shroud underside are achieved for 2.25 % coolant flow with a blowing ration of about 1.5 (Figure 11c). This has mainly two causes. The first is related to the increased blowing ratio. The coolant layer near the stator casing has a higher momentum than the main passage flow. This leads to an underturning of the coolant in the rotor passage. The coolant flow penetrates much further towards the pressure side of the blade and provides excellent effectiveness values near the pressure side of the blade trailing edge. However, only a small improvement is achieved near the trailing edge on the suction side. The CFD predicts even slightly lower effectiveness values in this region due to a more pronounced underturning of the coolant flow. The second reason for the more uniform coverage is the increased thickness of the coolant layer. The fluid that is swallowed at the pressure side of the shroud inlet cavity represents only a proportion of the coolant layer. The remainder is convected onto the shroud pressure side and provides effectiveness values similar to those on the shroud suction side.

Cooling effectiveness on blade surfaces

It was suggested in the previous section that the coolant trajectory on the shroud underside is influenced by the rotor secondary flow for low coolant flow rates and vice versa for the high coolant flow rates. The coolant distribution on the rotor blade surfaces gives further evidence for this effect. The measured results are presented from 70 % to 95 % of blade span in Figure 12.

Figure 12a shows that the blade pressure side remains completely uncooled for 0.75 % coolant mass flow rate. The

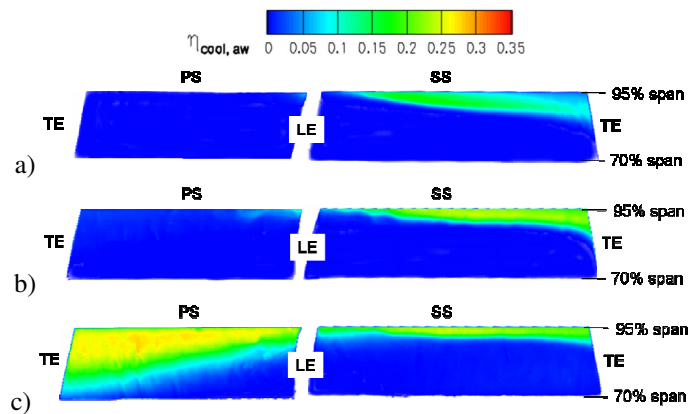


Figure 12 Cooling effectiveness on the tip section of the rotor blade; a) 0.75 %; b) 1.5 % and c) 2.25 % coolant flow rate

suction side of the blade is slightly cooled in the near shroud region. This coolant originates from the overturned shroud suction side boundary layer and accumulates on the suction side of the blade. It takes the typical path of low momentum fluid and is swept along the blade suction surface away from the shroud. The situation is very similar to that for 1.5 % coolant flow (Figure 12b). However, the radial extent of coolant coverage on the blade suction side is lower suggesting that the overturning is slightly reduced.

The coolant trajectory changes significantly for the case of 2.25 % coolant mass flow rate in Figure 12c. The high momentum coolant flow is underturned near the shroud. It penetrates deep towards the pressure side of the blade where it deflects radially inwards. The spanwise coverage on the suction side is further reduced. This shows that the rotor secondary flow near the shroud underside is initially reversed for the highest coolant flow rate.

Averaged cooling effectiveness results

The averaged cooling effectiveness values on the shroud (excluding the blade surfaces) are shown in Figure 13. Between 0.75 % and 1.75 % coolant mass flow rate, the effectiveness values increase almost linearly with the coolant mass flow rate. For higher flow rates, the trend levels off and starts to decrease

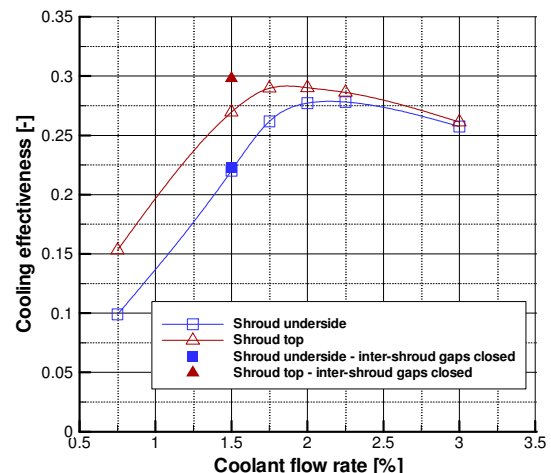


Figure 13 Averaged cooling effectiveness values on the shroud (Steady CFD, k-ε model)

above 2.25 %. This is explained by the high blowing ratio of the coolant jets. They penetrate deep into the passage and undergo strong mixing with the main passage flow. The result is a thick coolant layer around the shroud with concentration values that do not exceed 30 %. Higher cooling effectiveness values could only be achieved by decreasing the blowing ratio for the high coolant flow rates as this decreases the penetration depth and the mixing.

Figure 13 shows also the results for closed inter shroud gaps at the design coolant flow rate. On the shroud top surfaces, the leakage flow through the gaps results in a reduction of cooling effectiveness of about 10 %. On the shroud underside the effect is less severe and amounts to about 2 %.

SUMMARY AND CONCLUSIONS

The experimental and numerical results presented in this paper give insight into the aerothermal performance of the shroud of a high pressure turbine blade. A primary determination is that the Nusselt numbers on the suction side of the shroud are approximately twice as high as on the shroud pressure side. This applies to the shroud top surfaces as well as to the shroud underside. On the shroud top, the highest values are seen near the inter-shroud gap where the shroud cavity vortices drive the tip leakage jets onto the rear of the fins and the cavity bottom surfaces. The regions of highest Nusselt numbers correlate well with the flow attachment regions observed from the PIV and the flow visualisation.

The highest Nusselt numbers on the shroud underside are found in the stagnation region near the shroud leading edge and on the suction side part of the shroud. The latter is due to the higher velocities in the suction side part of the passage and the influence of the inter-shroud gap. The pressure side part of the shroud underside was found to be the region of lowest Nusselt numbers on the entire shroud.

The measurements and predictions of the adiabatic cooling effectiveness have produced two main conclusions. First, the Platform-Cooling methodology performs best for blowing ratios of unity and slightly higher in terms of the uniformity of coolant coverage and the effectiveness values. Blowing ratios significantly lower than unity lead to overturning of the coolant in the passage. Higher blowing ratios lead to underturning of the coolant flow and a migration (loss) of coolant towards midspan positions in the rotor passage on the pressure side of the blade. Second, the coolant distribution on the shroud underside is significantly affected by the inflow/outflow pattern at the shroud inlet cavity. Especially for the lower coolant flow rates, only low levels of cooling can be achieved on the pressure side of the shroud underside.

As in the cases of the aerodynamic and the heat transfer results, the inter-shroud gaps have also negative effects on the cooling performance on the shroud surfaces. On the shroud underside, some of the coolant film is sucked into the inter-shroud gap, thus decreasing the cooling effectiveness on the suction side part of the adjacent blade. As this leakage flow has lower coolant concentrations compared to the cavity flow, it also reduces the effectiveness values in the shroud cavities.

Both effects are more pronounced for the lower coolant flow rates.

ACKNOWLEDGEMENTS

This research was conducted within the European research project AITEB-2, 6FP, AST4-CT-2005-516113. The authors wish to thank all members of the AITEB-2 consortium and the European Commission for funding this research work. In addition the authors are grateful for the cooperation with Vassilis Stefanis of ALSTOM regarding the generation of the computational mesh.

REFERENCES

- [1] Lehmann, K., Kanjirakkad, V. P., Hodson, H. P., 2011 "Aerodynamic and Aerothermal investigation of the flow around an HPT Rotor Shroud: PIV Measurements", ASME Turbo Expo, GT2011-45977
- [2] Kanjirakkad, V. P., Thomas, R. L., Hodson, H. P., Janke, E., Haselbach, F., Whitney, C., 2008 "Passive Shroud Cooling Concepts for HP Turbines: Experimental Investigations", Journal of Turbomachinery, Vol. 130,1
- [3] Janke, E., Haselbach, F., Whitney, C., Kanjirakkad, V. P., Thomas, R. L., Hodson, H. P., 2006 "Passive Shroud Cooling Concepts for HP Turbines: CFD based Design Approach", ASME IGTI Turbo Expo, GT2006-91194
- [4] Waschka, W., Wittig, S., Kim, S., Scherer, T., 1993 "Heat Transfer and Leakage in High-Speed Rotating Stepped Labyrinth Seals," AGARD Conference Proceedings 527, Heat Transfer and Cooling in Gas Turbines
- [5] Wittig, S., Jacobsen, K., Schelling, U., Kim, S., 1988, "Heat Transfer in Stepped Labyrinth Seals", Journal of Engineering for Gas Turbines and Power, Vol. 110, pp. 63-69
- [6] Haller, B. R., Hilditch, M. A., "External Heat Transfer on a Shrouded HP Gas Turbine Stage", ASME IGTI Turbo Expo, GT2007-27168
- [7] Lehmann, K., Thomas, R., Hodson, H. P., Stefanis, V., 2009, "Heat Transfer and Aerodynamics of Over-Shroud Leakage Flows in a High Pressure Turbine", ASME Turbo Expo, GT2009-59531
- [8] Lehmann, K., 2010, "Heat Transfer and Aerodynamics of Over-Shroud Leakage Flows in a High Pressure Turbine", PhD Thesis, University of Cambridge
- [9] Friedrichs, S., Hodson, H. P., Dawes, W. N., 1996, "Distribution of Film-Cooling Effectiveness on a Turbine Endwall Measured Using the Ammonia and Diazo Technique", ASME Journal of Turbomachinery, Vol. 118, pp 613-621